

Isotope Effects in 2D correlation infrared Spectra of Water: HEOM Analysis of Molecular Dynamics–Based Machine Learning Models

Kwanghee Park[✉], Ryotaro Hoshino[✉], and Yoshitaka Tanimura^{✉^a}

Department of Chemistry, Graduate School of Science, Kyoto University, Kyoto 606-8502, Japan

(Dated: Last updated: 20 March 2026)

We model, simulate, and analyze the intramolecular modes of liquid H₂O and D₂O to elucidate how energy excitation, relaxation, and vibrational dephasing interplay through anharmonic mode-mode coupling. Our analysis employs two-dimensional (2D) correlation spectra, a representative observable in nonlinear infrared vibrational spectroscopy. Accurate reproduction of these 2D spectral profiles requires not only a precise dynamical description of intramolecular vibrations but also an appropriate treatment of thermal environmental effects arising from strong interactions with surrounding molecules, which act as thermal baths. Capturing the essential features of the 2D spectra further demands a non-Markovian, non-perturbative, and nonlinear description of the interactions between intramolecular modes and their baths. To this end, we adopt a hierarchical equations of motion (HEOM) framework to compute the 2D spectra. By comparing the resulting spectra of H₂O and D₂O, we explore the underlying mechanisms governing their complex energy and phase relaxation dynamics.

I. INTRODUCTION

Water molecules possess a simple molecular structure, yet the collective dynamics mediated by hydrogen bonding are remarkably complex, underpinning a wide range of chemical reactions and biological processes.¹ Isotope substitution provides a fundamental means of probing these intricate dynamics. Replacing H₂O with D₂O modifies zero-point energies and vibrational couplings, leading to measurable changes in spectral line shapes, coherence lifetimes, and reaction kinetics. Such isotope-dependent variations have been exploited to elucidate hydrogen-bonding networks,² clarify tunneling contributions,³ and refine mechanistic models of aqueous reactions.⁴ Ultrafast spectroscopic techniques, including X-ray free-electron laser experiments, offer direct access to the quantum properties of hydrogen-bonded liquids by probing femtosecond dynamics and isotope-dependent vibrational coupling.⁵ In particular, two-dimensional vibrational spectroscopy (2DVS)^{6–18} has proven to be a powerful approach for investigating isotope effects, as it provides direct experimental evidence for vibrational coherence dynamics and their lifetimes within hydrogen-bonded water networks.^{19–23}

Recent theoretical studies have further shown that sparse hydroxyl solutes (e.g., HOD in liquid D₂O) serve as clean spectroscopic probes of the local hydrogen-bonding environment, owing to the OH stretching vibration’s relative isolation from other modes.^{24–34} Molecular dynamics (MD) simulations combined with empirical mappings between local electric fields and OH stretching frequencies have yielded valuable insights into IR, Raman, and 2D IR spectra.^{35–41} However, discrepancies

remain, particularly in spectral linewidths and echo peak-shift dynamics, highlighting the limitations of empirical frequency-field correlations and classical approximations in capturing the quantum nature of environmental interactions and spectral diffusion.^{42–44}

Given the inherent difficulty of simulating nonlinear spectroscopy within a quantum MD framework, we have recently developed a suite of computational tools designed to overcome this challenge. These tools employ machine-learning (ML) techniques to parameterize a multimodal anharmonic Brownian (MAB) model directly from MD trajectories (`sbml4md`).^{45–47} The resulting model provides a physically transparent platform for analyzing the roles of anharmonicity, energy relaxation, and vibrational dephasing as they interplay through anharmonic mode-mode coupling among intramolecular modes.

Capturing the essential features of the 2D spectra further demands a non-Markovian, non-perturbative, and nonlinear description of the interactions between intramolecular modes and their baths in both classical and quantum regimes.⁴⁸ Therefore, in parallel with this research, our group developed a computational platform capable of rigorously treating (i) any two quantum inter- and intramolecular modes (DHEOM-MLWS),^{49,50} (ii) any three classical inter- and intramolecular modes (CHFPE-2DVS),^{51,52} and (iii) three quantum intramolecular modes (HEOM-2DVS),⁵³ thereby enabling the numerical computation of 2DVS. By combining these tools, we can model various solutions, including water, and obtain spectra such as 2D IR-Raman and 2D IR as needed. In this paper, we utilize this framework to model, simulate, and analyze the 2D correlation spectroscopy of H₂O and D₂O, thereby clarifying the underlying mechanisms governing their complex energy and phase relaxation dynamics.

This paper is organized as follows. Section II introduces our strategy, which combines MD and ML to pa-

^a) Author to whom correspondence should be addressed: tanimura.yoshitaka.5w@kyoto-u.jp

parameterize the MAB model and compute 2D IR spectra via HEOM: MD \rightarrow ML (sbml4md) \rightarrow MAB model \rightarrow 2D IR (CHFPE-2DVS/HEOM-2DVS). Section III explains simulation details. Then Sec. IV presents the evaluated parameter values of the MAB model for H₂O and D₂O, along with the linear absorption and 2D correlation IR spectra calculated from them. Section V is devoted to the summary.

II. MD SIMULATION, ML-BASED MAB MODELING, AND 2D IR VIA HEOM

Here, we briefly describe our complementary strategy for constructing data-driven models from atomic trajectories and for computing 2DVS by solving them within the HEOM framework. Figure 1 summarizes the workflow used in this study. For clear illustration, we restrict the present discussion to the intramolecular modes of water, although the approach is in principle applicable to any solvent-solute system or to reaction centers within biomolecules.

A. MAB model

At the core of our approach is the MAB model. In this paper, we consider the three primary intramolecular modes of the water molecule: (1) anti-symmetric stretch, (1') symmetric stretch, and (2) bending. These modes are described by dimensionless vibrational coordinates $\mathbf{q} = (q_1, q_{1'}, q_2)$. Each mode is independently coupled to the other optically inactive modes, which constitute a bath system represented by an ensemble of harmonic oscillators. The total Hamiltonian can then be expressed as^{45–47,49–55}

$$\hat{H}_{tot} = \sum_s \left(\hat{H}_A^{(s)} + \hat{H}_I^{(s)} + \hat{H}_B^{(s)} + \hat{H}_C^{(s)} \right) + \frac{1}{2} \sum_{s \neq s'} \hat{U}_{ss'}(\hat{q}_s, \hat{q}_{s'}), \quad (1)$$

where

$$\hat{H}_A^{(s)} = \frac{\hat{p}_s^2}{2m_s} + \hat{U}_s(\hat{q}_s) \quad (2)$$

is the Hamiltonian for the s th mode ($s = 1, 1',$ and 2), with mass m_s , coordinate \hat{q}_s , and momentum \hat{p}_s ; and

$$\hat{U}_s(\hat{q}_s) = \frac{1}{2} m_s \omega_s^2 \hat{q}_s^2 + \frac{1}{3!} g_{s^3} q_s^3 \quad (3)$$

is the anharmonic potential for the s th mode, described by the frequency ω_s and cubic anharmonicity g_{s^3} . The mode-mode coupling between the s th and s' th modes is given as

$$\hat{U}_{ss'}(\hat{q}_s, \hat{q}_{s'}) = g_{ss'} \hat{q}_s \hat{q}_{s'} + \frac{1}{6} (g_{s^2 s'} \hat{q}_s^2 \hat{q}_{s'} + g_{ss'^2} \hat{q}_s \hat{q}_{s'}^2), \quad (4)$$

where $g_{ss'}$ represents the second-order harmonicity, and $g_{s^2 s'}$ and $g_{ss'^2}$ represent the third-order anharmonicity. In the third-order response function considered below, the contributions from even-order anharmonicity vanish.⁵⁶ Therefore, here we retain only the third-order anharmonic terms.

The bath Hamiltonian for the s th mode is expressed as^{57,58}

$$\hat{H}_B^{(s)} = \sum_{j_s} \left(\frac{\hat{p}_{j_s}^2}{2m_{j_s}} + \frac{m_{j_s} \omega_{j_s}^2 \hat{x}_{j_s}^2}{2} \right), \quad (5)$$

where the momentum, coordinate, mass, and frequency of the j_s th bath oscillator are given by p_{j_s} , x_{j_s} , m_{j_s} and ω_{j_s} , respectively. The counter term is expressed as^{59,60}

$$\hat{H}_C^{(s)} = \Lambda^{(s)} \hat{V}_s^2(\hat{q}_s) \quad (6)$$

with $\Lambda^{(s)} \equiv \sum_{j_s} \alpha_{j_s}^2 / 2m_{j_s} \omega_{j_s}^2$. The system-bath (S-B) interaction, defined as

$$H_I^{(s)} = -V_s(\hat{q}_s) \sum_{j_s} \alpha_{j_s} \hat{x}_{j_s}, \quad (7)$$

consists of linear-linear (LL)^{61,62} and square-linear (SL) S-B interactions,^{60,63,64} $V_s(\hat{q}_s) \equiv V_{LL}^{(s)} \hat{q}_s + V_{SL}^{(s)} \hat{q}_s^2/2$, with coupling strengths $V_{LL}^{(s)}$, $V_{SL}^{(s)}$, and α_{j_s} . For a vibrational mode with weak anharmonicity, the LL interaction leads to energy relaxation, while the SL interaction results in vibrational dephasing.^{57,63}

The bath property is characterized by the spectral distribution function (SDF), defined as $J_s(\omega) \equiv \sum_{j_s} (\alpha_{j_s}^2 / 2m_{j_s} \omega_{j_s}) \delta(\omega - \omega_{j_s})$. To employ the HEOM formalism, we consider the Drude SDF,

$$J_s(\omega) = \frac{m_s \zeta_s}{2\pi} \frac{\gamma_s^2 \omega}{\omega^2 + \gamma_s^2}. \quad (8)$$

The factor of the counter term is now given by

$$\Lambda^{(s)} = \frac{m_s \zeta_s \gamma_s}{2}. \quad (9)$$

B. Generation of MD Trajectories

The parameter variables of the MAB model are evaluated based on atomic trajectories generated by MD simulations. Several important considerations are summarized below.^{65–67}

System size. Because we aim to model fast intermolecular modes that originate from short-range intermolecular interactions, it is not necessary to perform large-scale simulations with many molecules. Thus, relatively small system sizes are sufficient, and even systems containing 200–300 molecules reproduce the qualitative behavior of liquid water.

Thermostat effects. Because 2DIR signals are highly sensitive to molecular dynamics, the use of thermostats

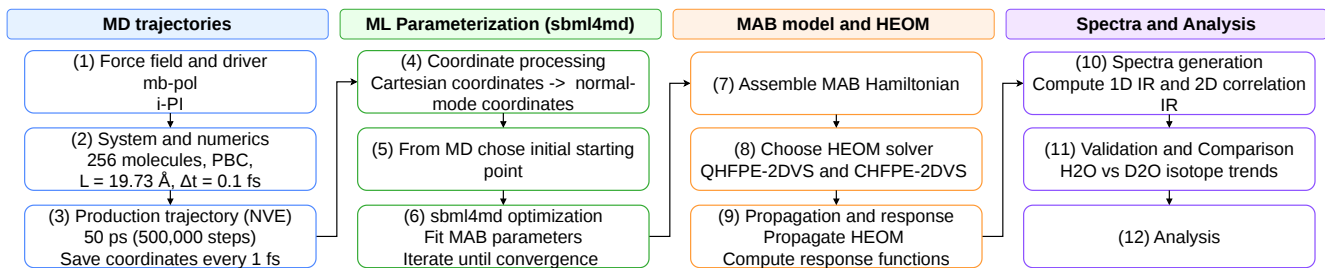


FIG. 1. Overall workflow used in this study: MD trajectory generation, ML-based parameterization of the MAB model (sbml4md), assembly of the S-B Hamiltonian, CHFPE/HEOM propagation, and construction/analysis of 1D and 2D correlation IR spectra.

such as the Nosé-Hoover or Langevin schemes can distort the 2D spectral profiles, particularly along the t_2 waiting-time axis. For accurate dynamical behavior, microcanonical (NVE) simulations are therefore preferred.

Force-field dependence. The 2DIR response strongly depends on the accuracy of the force field. Differences in anharmonicity or structural fidelity lead to noticeable changes in the nonlinear response, even for nonpolar systems. Reliable force fields should therefore be validated against experimental structural data.

Long-range treatment of induced polarizability. The 2DIR profile is sensitive to the functional form of the induced polarizability. For many molecular systems, the Ewald summation is required to properly account for long-range dipole-dipole interactions, although the magnitude of the effect depends on the molecule.

Atomic trajectories for machine learning. For liquid water, a training trajectory has a total length of approximately 50 ps, with Cartesian coordinates of all atoms in all molecules saved every 10 steps (1 fs) with an integration time step of 0.1 fs. The required length of the underlying MD trajectory is evaluated from the linear absorption spectrum obtained directly from the simulation. Accurately reproducing the bending-mode peak requires a longer trajectory than that needed to capture the stretching-mode peak.

Notes for other molecular systems. Although the discussion above focuses on liquid water, similar considerations apply to other molecular systems. The required trajectory length, the sensitivity to thermostating, and the importance of long-range electrostatics all depend on the characteristic timescales and interaction strengths of the system under study. For systems with slower structural relaxation or stronger intermolecular correlations, substantially longer MD trajectories may be necessary to achieve converged spectral features. Careful validation against experimental observables is therefore essential when extending the MAB parameterization to different molecular environments.

C. ML procedure (sbml4md)

The dynamical characteristics of the MAB model are defined by several key components: the vibrational potentials of the individual modes, the anharmonic mode-mode couplings, the functional forms of the linear and nonlinear interactions between the modes and the bath, and, critically, the SDF that governs the bath fluctuations. In our approach, these interaction forms are specified in advance, and their corresponding dynamical parameters are determined through ML optimization. The bath, treated as a continuum of degrees of freedom, is represented by a set of harmonic oscillators—typically numbering more than one thousand—whose coupling constants are optimized to reproduce the MD results, from which the SDF parameters are subsequently inferred. With these elements in place, the algorithm developed by our group (sbml4md) proceeds for the intramolecular vibrations of liquid water as a representative example.

1. Intramolecular Modes

By representing the molecular environment as a continuous function $J(\omega)$ defined by Eq. (8), we have effectively considered a low-temperature heat bath with infinite specific heat, modeled by an infinite number of harmonic oscillators. In our description, the intramolecular modes (1), (1') and (2) are described in terms of the two O-H bond lengths and the H-O-H bond angle of the k th water molecule, defined as

$$r_1^k = |\mathbf{x}_O^k - \mathbf{x}_{H_1}^k|, \quad (10)$$

$$r_2^k = |\mathbf{x}_O^k - \mathbf{x}_{H_2}^k|, \quad (11)$$

and

$$\theta^k = \arccos \left(\frac{(\mathbf{x}_O^k - \mathbf{x}_{H_1}^k) \cdot (\mathbf{x}_O^k - \mathbf{x}_{H_2}^k)}{r_1^k r_2^k} \right), \quad (12)$$

where \mathbf{x}_O , \mathbf{x}_{H_1} , and \mathbf{x}_{H_2} are the positions of the oxygen, the 1st, and 2nd hydrogen atoms, respectively, describing

the intramolecular motion of the k th molecule and r_1 and r_2 are the average length of r_1^k and r_2^k

The system coordinates for three intramolecular modes are expressed as

$$q_1^k = \frac{1}{2} (r_1^k - r_2^k), \quad (13)$$

$$q_{1'}^k = \frac{1}{2} (r_1^k + r_2^k - 2r_0), \quad (14)$$

$$q_2^k = \theta^k - \theta_0, \quad (15)$$

where the equilibrium values of r_0 and θ_0 are evaluated from the equilibrium distributions as $\langle r \rangle$ and $\langle \theta \rangle$. The system and S-B interaction, $H_B^{(s)}$ and $H_I^{(s)}$, are described with these system coordinates. The intramolecular mode-mode interaction, $U_{s,s'}(q_s, q_{s'})$, in the system Hamiltonian can be obtained by rewriting the intramolecular potentials appearing in Eqs.(3) and (4) in terms of Eqs. (13)-(15), respectively.

2. Bath oscillators

The degrees of freedom associated with the surrounding molecular motions, including the representative intermolecular vibrational mode, are treated as bath oscillators and are described by $H_I^{(s)}$ and $H_B^{(s)}$, given in Eqs. (5) and (7), respectively.

Within the ML framework, introducing a bath with infinitely many degrees of freedom is not feasible. Consequently, the bath coupled to the s th mode is represented by a system of N_s finite harmonic oscillators. The inverse of the interval $\Delta\omega_{N_s}$ between the eigenenergies of these oscillators determines the required sampling time of the trajectory, with longer times needed for smaller intervals. In practice, N_s is typically chosen between 1000 and 2000.

Under this prescription, the trajectory of the j_s th oscillator is given by

$$\tilde{x}_{j_s}(t) = A_{j_s} \sin(\omega_{j_s} t + \phi_{j_s}), \quad (16)$$

where ϕ_{j_s} is a random phase and A_{j_s} is a parameter learned within the ML framework. The amplitudes of the bath oscillators $\{A_{j_s}\}$ are utilized to determine the Drude SDF parameters (λ_s, γ_s), and $\{A_{j_s}\}$ are updated consistently with SDF throughout training. Because the SDF is defined through the anti-symmetric function of $\tilde{x}_{j_s}(t)$ as $\sum_{j_s} \langle \{\tilde{x}_{j_s}(t'), \tilde{x}_{j_s}(t)\} \rangle$, where $\{\cdot, \cdot\}$ denotes the Poisson bracket,⁵⁷ the SDF must be optimized with respect to $\langle \{V_s(t'), V_s(t)\} \rangle$ rather than the operator $V_s(\hat{q}_s) = V_{LL}^{(s)} \hat{q}_s + V_{SL}^{(s)} \hat{q}_s^2/2$. This indicates that $V_{SL}^{(s)}$ cannot be determined independently of the Drude SDF strength ζ .

Because the overall scale of the SL coupling can be absorbed into the bath strength, there is a scale redundancy between the S-B coupling strength and $V_{SL}^{(s)}$. To make this explicit, we factor out the SL coefficient and

rewrite the interaction operator as $\hat{V}_s = V_{SL}^{(s)} (\hat{q}_s^2 + \bar{V}_{LL}^{(s)} \hat{q}_s)$ with $\bar{V}_{LL}^{(s)} \equiv V_{LL}^{(s)}/V_{SL}^{(s)}$.

We then optimize the coefficients through

$$c_{j_s}^k = \alpha_{j_s} V_{LL}^{(s)} A_{j_s}, \quad (17)$$

which allows $\bar{V}_{LL}^{(s)}$ to vary separately. We subsequently fix the gauge by applying a post-training normalization $V_{SL}^{(s)} \rightarrow 1$ and absorb its magnitude into the bath-strength parameter as $\zeta_s \rightarrow \zeta_s (V_{SL}^{(s)})^2$.

In the SL-only calculations reported in this work, we set $V_{LL}^{(s)} = 0$, so that $\bar{V}_{LL}^{(s)} = 0$ and the coupling operator reduces to $\hat{V}_s = \hat{q}_s^2/2$ after normalization.

The bath parameters and S-B couplings are then encoded in the latent variables

$$\mathbf{z}_k = \left(\{c_{j_1}^k\}, \{c_{j_1'}^k\}, \{c_{j_2}^k\} \right), \quad (18)$$

where $\{c_{j_s}^k\}$ denotes the set of bath-coupling parameters.

3. ML optimization

The trajectory of each molecule at time step i is then propagated using the MAB model:

$$\begin{aligned} (\tilde{\mathbf{q}}^k(t_0 + i\Delta t), \tilde{\mathbf{p}}^k(t_0 + i\Delta t)) &= \hat{L}(\Delta t; \mathbf{z}_k, \Sigma) \\ &\times (\tilde{\mathbf{q}}^k(t_0 + (i-1)\Delta t), \tilde{\mathbf{p}}^k(t_0 + (i-1)\Delta t)), \end{aligned} \quad (19)$$

where $(\tilde{\mathbf{q}}^k(t), \tilde{\mathbf{p}}^k(t))$ denote the coordinates and momenta of the k th molecule. The operator $\hat{L}(\Delta t; \mathbf{z}_k, \Sigma)$ is the Liouvillian corresponding to Eqs. (1)–(7) with the discretized heat bath, and Σ denotes the set of system and bath parameters.

For each molecule, phase-space trajectories $(\mathbf{q}^k(t), \mathbf{p}^k(t))$ from MD are compared with MAB-predicted trajectories $(\tilde{\mathbf{q}}^k(t), \tilde{\mathbf{p}}^k(t))$. Parameters in Eqs.(3) and (4) and the SDF Eq. (8) are optimized to reproduce the reference MD data. We define the loss function as the Mean Squared Error (MSE) between the predicted and actual MD trajectories for the s th mode:

$$\text{MSE}_{q_s} \equiv \frac{1}{N} \sum_{i=1}^N [\tilde{q}_s^k(t_i) - q_s^k(t_i)]^2. \quad (20)$$

Minimization of the above loss functions corresponds to the optimization of the learning model parameters. These include the anharmonicity of the potential energy surfaces, anharmonic mode-mode couplings, coupling strengths for LL and SL interactions, and the SDF parameters associated with each vibrational mode.

To optimize the MAB model parameters, we employ a generative ML scheme:

1. Read generated MD trajectories of water molecules from the input file.

2. Simulate corresponding trajectories with the MAB model under trial parameters.
3. Compute a loss function measuring deviation from MD references.
4. Backpropagate the loss to iteratively refine parameters.

D. CHFPE-2DVS

Once the MAB variables are obtained, the spectrum is calculated using the HEOM framework. For Eqs. (1)–(9) with the Drude SDF [Eq. (8)], CHFPE-2DVS⁵¹ and QHFPE-2DVS⁵³ have been established to treat three vibrational modes to simulate 2D correlation IR spectra.

In the CHFPE-2DVS, the terms associated with the Matsubara frequencies vanish, and the equations are expressed as follows^{51,52,55}

$$\begin{aligned} \frac{\partial W^{(\mathbf{n})}(\mathbf{q}, \mathbf{p}; t)}{\partial t} &= (\hat{L}(\mathbf{q}, \mathbf{p}) - \sum_s n_s \gamma_s) W^{(\mathbf{n})}(\mathbf{q}, \mathbf{p}; t) \\ &+ \sum_s \hat{\Phi}_s W^{(\mathbf{n}+\mathbf{e}_s)}(\mathbf{q}, \mathbf{p}; t) \\ &+ \sum_s \hat{\Theta}_s W^{(\mathbf{n}-\mathbf{e}_s)}(\mathbf{q}, \mathbf{p}; t), \end{aligned} \quad (21)$$

where $W^{(\mathbf{n})}(\mathbf{q}, \mathbf{p}; t)$ is the Wigner distribution function (WDF) and the hierarchical elements are denoted as $\mathbf{n} = (n_1, n_{1'}, n_2)$, where each n_s is a non-negative integer representing the s th mode, and \mathbf{e}_s is the unit vector in the s th mode. Note that $W^{(\mathbf{n})}(\mathbf{q}, \mathbf{p}; t)$ has physical meaning only when $\mathbf{n} = (0, 0, 0)$; for all other values of \mathbf{n} , it serves as an auxiliary WDF that accounts for non-perturbative and non-Markovian S-B interactions.^{57,58}

The classical Liouvillian \hat{L} corresponding to the system Hamiltonian $H_{\text{sys}}(\mathbf{q}, \mathbf{p}) \equiv \sum_s H_A^{(s)} + \sum_{s < s'} U_{ss'}(\hat{q}_s, \hat{q}_{s'})$ is defined as

$$\hat{L}(\mathbf{q}, \mathbf{p})W(\mathbf{q}, \mathbf{p}) \equiv \{H_{\text{sys}}(\mathbf{q}, \mathbf{p}), W(\mathbf{q}, \mathbf{p})\}_{\text{PB}}, \quad (22)$$

where $\{\cdot, \cdot\}_{\text{PB}}$ denotes the Poisson bracket, given by

$$\{A, B\}_{\text{PB}} \equiv \sum_s \left(\frac{\partial A}{\partial q_s} \frac{\partial B}{\partial p_s} - \frac{\partial A}{\partial p_s} \frac{\partial B}{\partial q_s} \right) \quad (23)$$

for any functions A and B .

The operators $\hat{\Phi}_s$ and $\hat{\Theta}_s$ describe the energy exchange between the s th mode and its corresponding bath, and are defined as follows:^{63,64}

$$\hat{\Phi}_s = \frac{\partial V_s(q_s)}{\partial q_s} \frac{\partial}{\partial p_s}, \quad (24)$$

and

$$\hat{\Theta}_s = \frac{m_s \zeta_s \gamma_s}{\beta} \frac{\partial V_s(q_s)}{\partial q_s} \frac{\partial}{\partial p_s} + \zeta_s \gamma_s p_s \frac{\partial V_s(q_s)}{\partial q_s}, \quad (25)$$

where ζ_s is the S-B coupling strength, γ_s is the inverse correlation time, and T is the temperature.

E. HEOM-2DVS

The system Hamiltonian can always be expressed in matrix form using the energy eigenstates of $\hat{H}_A^{(s)}$, denoted as $|n\rangle_s$ with eigenenergy $\hbar\omega_n^s = {}_s\langle n | \hat{H}_A^{(s)} | n' \rangle_s$. Then for $\hat{H}_S \equiv \sum_s \hat{H}_A^{(s)} + \sum_{s < s'} \hat{U}_{ss'}(\hat{q}_s, \hat{q}_{s'})$ we have

$$\begin{aligned} \hat{H}_S &= \hbar \sum_s \sum_n \omega_n^s |n\rangle_{ss} \langle n| \\ &+ \hbar \sum_{s < s'} \sum_{n \neq n'} \Delta_{nn'}^{ss'} |m\rangle_{s'} |n\rangle_{ss} \langle n'|_{s'} \langle m'| \end{aligned} \quad (26)$$

where $\hbar\Delta_{nn'}^{ss'} = {}_s\langle n | s' \langle m' | \hat{U}_{ss'}(\hat{q}_s, \hat{q}_{s'}) | n' \rangle_s | m' \rangle_{s'}$.

The system part of the S-B interaction is expressed as

$$\hat{V}_s = \sum_{n \geq n'} V_{nn'}^s |n\rangle_{ss} \langle n'|, \quad (27)$$

where $V_{nn'}^s \equiv {}_s\langle n | V_s(\hat{q}_s) | n' \rangle_s$.

The HEOM obtained by transforming the phase-space representation into the energy-eigenvalue representation differs from the standard HEOM in that it requires explicitly including the counter term

$$\hat{H}_C = \hbar \sum_s \sum_{n \geq n'} \delta_{nn'}^s |n\rangle_{ss} \langle n'| \quad (28)$$

with

$$\hbar\delta_{nn'}^s = \frac{m_s \zeta_s \gamma_s}{2} {}_s\langle n | V_s^2(\hat{q}_s) | n' \rangle_s \quad (29)$$

as $\hat{H}'_S \equiv \hat{H}_S + \hat{H}_C$ in the system Hamiltonian.

Here and hereafter, we define the hyperoperators $\hat{A}^\times \hat{B} \equiv \hat{A}\hat{B} - \hat{B}\hat{A}$ and $\hat{A}^\circ \hat{B} \equiv \hat{A}\hat{B} + \hat{B}\hat{A}$, for arbitrary operators \hat{A} and \hat{B} . The HEOM-2DVS is then expressed as⁴⁶

$$\begin{aligned} \frac{d}{dt} \hat{\rho}_{\{\mathbf{n}_s\}} &= - \left[\frac{i}{\hbar} \hat{H}'_S{}^\times + \sum_s \sum_{k=0}^{K_s} (n_k^s \nu_k^s) \right] \hat{\rho}_{\{\mathbf{n}_s\}} \\ &- i \sum_s \sum_{k=0}^{K_s} n_k^s \hat{\Theta}_k^s \hat{\rho}_{\{\mathbf{n}_s - \mathbf{e}_s^k\}} \\ &- i \sum_s \sum_{k=0}^{K_s} \hat{V}_s{}^\times \hat{\rho}_{\{\mathbf{n}_s + \mathbf{e}_s^k\}}. \end{aligned} \quad (30)$$

The hierarchy elements are indexed by the set $\{\mathbf{n}_s\} \equiv (\mathbf{n}_1, \mathbf{n}_2, \mathbf{n}_3)$, where each \mathbf{n}_s is a multi-index defined as $\mathbf{n}_s = (n_0^s, n_1^s, \dots, n_{K_s}^s)$ for the three-mode case. All elements $\hat{\rho}_{\{\mathbf{n}_s\}}(t)$ with any negative index $n_k^s < 0$ are set to zero.

The notation $\{\mathbf{n}_s \pm \mathbf{e}_s^k\}$ indicates an increment or decrement of the k th component of \mathbf{n}_s , where \mathbf{e}_s^k is the unit vector corresponding to the k th frequency component in the s th bath. The operators are defined as follows:

$$\hat{\Theta}_0^{(s)} = -i \frac{m_s \zeta_s \gamma_s^2}{2} \hat{V}_s^{\circ} + \frac{m_s \zeta_s \gamma_s}{\beta \hbar} \left(1 + \sum_{k=1}^{K_s} \frac{2\eta_k^s \gamma_s^2}{\gamma_s^2 - \nu_k^2} \right) \hat{V}_s^{\times}, \quad (31)$$

and

$$\hat{\Theta}_{k>0}^{(s)} = -\frac{m_s \zeta_s \gamma_s^2}{\beta \hbar} \frac{2\eta_k^s \nu_k}{\gamma_s^2 - \nu_k^2} \hat{V}_s^{\times}, \quad (32)$$

where the parameters η_k^s denotes the Padé-approximated thermal coupling.⁶⁸

F. Linear absorption spectrum and 2D correlation IR spectra

For optical measurements in which the molecular system interacts with a laser field $E(t)$, the nonlinear components of the dipole moment are essential for describing 2D spectroscopy. Here we assume^{49–52,55}

$$\hat{\mu} = \sum_s \mu^s \hat{q}_s + \frac{1}{2!} \sum_{s,s'} \mu^{ss'} \hat{q}_s \hat{q}_{s'}, \quad (33)$$

where μ_s and $\mu_{ss'}$ denote the linear and nonlinear elements, respectively. In this work, the nonlinear elements $\mu^{ss'}$ were taken from Ref. 51. The linear elements μ^s primarily control the relative band strengths in the calculated 1D/2D signals; therefore, after fixing the MAB dynamical parameters, we refined μ^s by fitting the CHFPE-calculated 1D spectrum to the MD-derived 1D spectrum using an automated search procedure (described in Sec. IV A).

For the intramolecular three-mode vibration, the excitation frequency greatly exceeds thermal excitation, so the equilibrium state is taken as the ground state $|0\rangle = |0_1, 0_{1'}, 0_2\rangle$. Applying the dipole operator $\hat{\mu}$ yields the excited state $|1\rangle$, which contains single- and double-excitation components. A second application produces both returns to the ground state and higher excitations, collectively denoted as $|2\rangle$.⁵³

In the density operator representation, the first-order response function is^{57,58}

$$R^{(1)}(t_1) = \left(\frac{i}{\hbar} \right) \text{tr} \{ \hat{\mu} \mathcal{G}(t_1) \hat{\mu}^{\times} \hat{\rho}^{\text{eq}} \}, \quad (34)$$

where $\hat{\mathcal{G}}(t) \equiv \exp[-(i/\hbar)\hat{H}_{\text{tot}}^{\times}t]$, which represents the Green's function (Liouvillian propagator) of the system in the absence of a laser interaction, and $\hat{\rho}^{\text{eq}}$ is the equilibrium state.

The linear absorption spectrum is then evaluated as $I(\omega) = \int_0^{\infty} dt R^{(1)}(t) \exp(i\omega t)$. The third-order response is

$$R^{(3)}(t_3, t_2, t_1) = \left(\frac{i}{\hbar} \right)^3 \text{tr} \{ \hat{\mu} \mathcal{G}(t_3) \hat{\mu}^{\times} \mathcal{G}(t_2) \hat{\mu}^{\times} \mathcal{G}(t_1) \hat{\mu}^{\times} \hat{\rho}^{\text{eq}} \}, \quad (35)$$

which expands into more than sixteen terms for three energy eigenstates. These include both population states such as $|1\rangle\langle 1|$ and coherent states such as $|2\rangle\langle 1|$.

In 2D correlation spectroscopy, coherent contributions, such as $|2\rangle\langle 1|$ are excluded.^{69–71} Rephasing parts correspond to population states, while non-rephasing parts involve coherences. For density operators in the energy eigenbasis, separation is achieved by evaluating the specific Liouville pathways associated with excited-state populations and their conjugates, yielding the 2D correlation spectra. The detail of this procedure is explained in Refs. 53 and 58.

III. SIMULATION DETAILS

A. MD simulation

Intermolecular interactions were modeled with the `mb-pol` potential,^{38,39} a quantum-chemistry-based many-body framework that reproduces the properties of water across all phases with near-quantum-chemical accuracy. Training data were generated from molecular dynamics simulations performed with the `i-PI` driver,⁷² which was coupled to an external force engine via the socket interface under classical conditions.

Simulations were carried out for liquid H₂O and D₂O systems, each containing 256 molecules in a cubic box of side length 19.7295 Å under periodic boundary conditions. The MD trajectories were propagated in the micro-canonical (NVE) ensemble, initialized at 298.15 K. The equations of motion were integrated with a time step of 0.1 fs for a total of 500,000 steps (50 ps). Center-of-mass translational motion was removed to eliminate global drift associated with finite-precision integration. Cartesian coordinates were saved every 10 steps (1 fs), and thermodynamic quantities were recorded at each step. For D₂O, isotopic masses were explicitly assigned at initialization (O: 15.999 u, H: 1.008 u, D: 2.014 u).

B. ML parameterization

Based on the obtained MD trajectories, parameterization of the MAB model via ML was carried out following the procedure described in II C. In this work, we focus on the case in which V_{LL} is set to zero.

The thermal bath associated with each vibrational mode was represented by $N_s = 1500$ harmonic oscillators whose frequencies were defined as $\omega_{j_s} = j_s \Delta\omega$ with $\Delta\omega = 1 \text{ ps}^{-1} \approx 5.31 \text{ cm}^{-1}$. This frequency grid spans up to 8000 cm^{-1} , thereby covering the overtone region of the OH stretching mode. The initial phases $\phi_{j_s}^k$ were randomly sampled from a uniform distribution over $[0, 2\pi)$ at each iteration step.

The MAB Hamiltonian [Eq. (1)] was propagated using a time step of 0.1 fs. The latent variables \mathbf{z}_k were initialized to zero, and both the system parameters and

TABLE I. Optimized parameters of the three-mode MAB model with the SL interaction for isotopic water trained from **mb-pol** potential: (1) anti-symmetric stretch, (1') symmetric stretch, and (2) bending for H₂O and D₂O. Here, $\tilde{\zeta}_s$ denotes the normalized S-B coupling strength, and γ_s denotes the inverse correlation time of the bath fluctuations, $V_{\text{SL}}^{(s)}$ denotes the SL interaction ($V_{\text{LL}}^{(s)} = 0$), and \tilde{g}_{s^3} is the cubic anharmonicity for the s vibrational mode, respectively. We set the fundamental frequency to $\omega_0 = 4000 \text{ cm}^{-1}$. The normalized parameters were defined as $\tilde{\zeta}_s \equiv (\omega_0/\omega_s)^2 \zeta_s$, and $\tilde{g}_{s^3} \equiv (\omega_s/\omega_0)^3 g_{s^3}$. Nonlinear dipole elements are reproduced from J. Chem. Phys. 163, 172501 (2025), with the permission of AIP Publishing⁵¹ and given by $\tilde{\mu}_{11'} = 1.2 \times 10^{-2}$, $\tilde{\mu}_{12} = 0$, and $\tilde{\mu}_{1'2} = 0$ with $\tilde{\mu}_{ss} \equiv (\omega_0/\omega_s)^2 \mu_{ss}$.

	s	$\omega_s \text{ (cm}^{-1}\text{)}$	γ_s/ω_0	$\tilde{\zeta}_s$	$V_{\text{SL}}^{(s)}$	\tilde{g}_{s^3}
H ₂ O	1	3712	1.17×10^{-2}	5.65	1	-2.70×10^{-3}
	1'	3574	9.33×10^{-3}	4.58	1	-3.43×10^{-3}
	2	1663	1.24×10^{-2}	4.75×10^{-1}	1	-5.16×10^{-2}
D ₂ O	1	2706	1.17×10^{-2}	8.92	1	-7.10×10^{-3}
	1'	2626	1.21×10^{-2}	6.16	1	-8.08×10^{-3}
	2	1213	1.29×10^{-2}	3.38×10^{-1}	1	-1.17×10^{-1}

TABLE II. Optimized mode-mode coupling parameters of the three-mode MAB model for isotopic water trained from **mb-pol** potential: (1) anti-symmetric stretch, (1') symmetric stretch, and (2) bending modes. Here, we set $\tilde{g}_{s's} = g_{s's}(\omega_0/\omega_s)(\omega_0/\omega_{s'})$, $\tilde{g}_{s^2s'} = g_{s^2s'}(\omega_0/\omega_s)^2(\omega_0/\omega_{s'})$, and $\tilde{g}_{ss'2} = g_{ss'2}(\omega_0/\omega_s)(\omega_0/\omega_{s'})^2$.

	s - s'	$\tilde{g}_{ss'}$	$\tilde{g}_{s^2s'}$	$\tilde{g}_{ss'2}$
H ₂ O	1 - 1'	4.28×10^{-1}	1.98×10^{-3}	1.37×10^{-3}
	1 - 2	1.01	7.05×10^{-3}	1.45×10^{-2}
	1' - 2	1.06	5.88×10^{-3}	1.44×10^{-2}
D ₂ O	1 - 1'	7.99×10^{-1}	4.98×10^{-3}	4.48×10^{-3}
	1 - 2	1.90	1.89×10^{-2}	4.20×10^{-2}
	1' - 2	1.83	1.79×10^{-2}	3.51×10^{-2}

\mathbf{z}_k were iteratively optimized. A minibatch size of 25 trajectories was used for each epoch, and the same set of trajectories was employed throughout the optimization. Iterations were continued until convergence of the potential parameters was achieved. Because MAB parameter optimization is non-convex and sensitive to starting points, we used physically motivated initial values for the system and bath parameters.

Initial fundamental frequencies ω_s were set from the peak positions of the MD-derived linear absorption spectrum for each intramolecular mode, while the initial bath correlation times (γ_s^{-1}) and coupling strengths (ζ_s) were chosen to reproduce the qualitative linewidths and relaxation timescales observed in the MD trajectories. In practice, we found that the bending mode is particularly sensitive to the initial bath strength. When the initial value of ζ_2 for the bend is set too large, it induces an unphysically strong S-B coupling, which in turn leads to

an artificial splitting of the bending peak in the resulting 1D and 2D spectra. To avoid this failure, we performed a multi-start search over several initial parameter combinations (especially for ζ_2), and selected the converged solution that (i) achieves stable loss reduction during training and (ii) yields a single-band bending feature with a smaller optimized ζ_2 . This strategy improves robustness without changing the model form, and it is consistent with the physical expectation that the bend should not require anomalously strong S-B coupling to reproduce the MD reference.

Model training was performed using Python 3.9.18 in conjunction with TensorFlow 2.15 and CUDA 12.2. All computations were executed on a system equipped with an Intel Core i9-13900H CPU and an NVIDIA GeForce RTX 4070 GPU.

The model parameters obtained for the MAB are summarized in Tables I and II.

C. CHFPE-2DVS calculations

The CHFPE-2DVS⁵² is time-integrated using the fourth-order Runge-Kutta method. Equation (21) is discretized using the compact finite-difference scheme on a non-uniform mesh.

For numerical integration, the hierarchy is truncated according to the condition $\delta_{\text{tot}} > \Delta_{\mathbf{n}}/N$, where $N = \sum_s n_s$ and

$$\Delta_{\mathbf{n}} = \prod_s (n_s)^{-0.05} (k_B T m_s \zeta_s)^{n_s}. \quad (36)$$

By adjusting the number of hierarchical elements, the spectrum can be computed with the desired accuracy.

The entire integration routine is implemented in CUDA with the CUBLAS library and executed primarily on the GPU, while host-device memory transfers are minimized. The source code was run on NVIDIA GEFORCE RTX 3080 (10 GB VRAM) GPU boards hosted on a workstation equipped with an 11th Gen Intel(R) Core(TM) i9-11900.

D. HEOM-2DVS calculations

To employ HEOM-2DVS,⁵³ the vibrational Hamiltonian was discretized using the Lagrange-Hermite mesh method (LHMM; Hermite-DVR) with $(N_x, N_y, N_z) = (50, 50, 50)$ and mode-dependent coordinate scaling factors $\mathbf{h} = (h_x, h_y, h_z) = (0.5, 0.5, 0.75)$. Here, \mathbf{h} rescales the dimensionless Gauss-Hermite quadrature nodes $r_{d,j}$ to the physical coordinate grid via $q_{d,j} = h_d r_{d,j}$ ($d = x, y, z$), thereby setting the effective coordinate extent of the LHMM grid for each mode. The DVR product basis was truncated by the cut scheme with $\sum_{d=1}^3 n_d \leq 2$, which yields a 10-dimensional basis prior to final diagonalization. Cross-mode anharmonic couplings were then

included, and the Hamiltonian was diagonalized in this truncated basis. For the subsequent HEOM propagation, eigenstates with energies $E \leq 3.0$ (in the scaled unit defined by $\omega_0 = 4000 \text{ cm}^{-1}$) were retained, resulting in $N_{\text{vib}} = 8$ levels for H_2O and $N_{\text{vib}} = 9$ levels for D_2O . Each vibrational mode was coupled to an independent Drude bath, whose parameters are summarized in Tables I and II. The bath correlation functions were treated in the pure Drude form without Padé decomposition, i.e., the number of Padé terms was set to $K_s = 0$ for all modes. The HEOM was truncated using the tolerance criterion with $\delta_{\text{tot}} = 10^{-15}$. Time evolution was performed using a fourth-order Runge–Kutta integrator with linear-stability control (RK4LS) with a time step of $dt = 0.25 \text{ fs}$ at $T = 300 \text{ K}$. Linear absorption spectra were obtained from trajectories of length 1.2 ps, corresponding to 4800 propagation steps. For 2D correlation spectra, the third-order response functions were evaluated on t_1 and t_3 windows of 0.6 ps each (2400 steps per time axis), with waiting times $t_2 = \{1, 50, 100, 500\} \text{ fs}$.

IV. RESULTS AND DISCUSSIONS

A. Linear absorption spectra

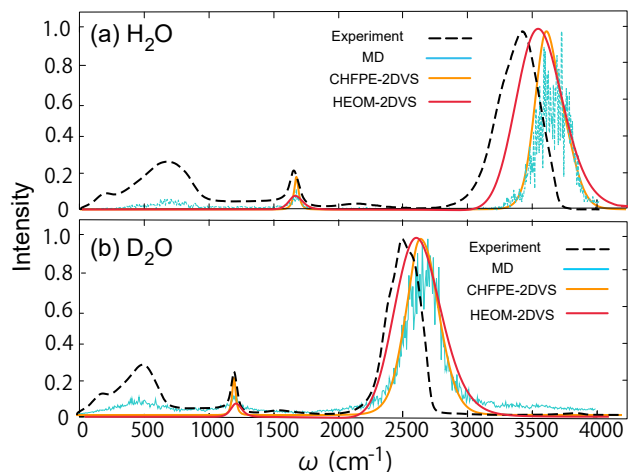


FIG. 2. Linear absorption spectra of (a) H_2O and (b) D_2O calculated using the three-mode MAB models with the parameter sets listed in Tables I and II. For comparison, each panel also includes results from MD simulations (blue lines) and experimental data (black dashed curves). Each spectrum is normalized to its maximum peak intensity. The H_2O experimental spectrum is reproduced with permission from Y. Maréchal, *J. Mol. Struct.* 1004, 146 (2011). Copyright (2011) Elsevier.⁷³ The D_2O experimental spectrum is reproduced from *J. Chem. Phys.* 131, 184505 (2009), with the permission of AIP Publishing.⁷⁴

The three-mode MAB parameters for H_2O and D_2O extracted from MD trajectories (Tables I and II) were used in the classical CHFPE-2DVS and quantum

HEOM-2DVS calculations. Figure 2 compares the resulting IR spectra with those obtained directly from MD trajectories and with experiment. To obtain the MD spectrum, we used the total dipole moment $\boldsymbol{\mu}^{\text{tot}}(t) = \boldsymbol{\mu}^{\text{perm}}(t) + \boldsymbol{\mu}^{\text{ind}}(t)$, evaluated at each sampling step. After removing the time-averaged dipole $\langle \boldsymbol{\mu}^{\text{tot}} \rangle$, we applied a real-valued FFT to each Cartesian component. The IR intensity was then computed as $I(\omega) \propto \omega^2 \sum_{\alpha=x,y,z} |\mu_{\alpha}^{\text{tot}}(\omega)|^2$.

Note that to match the relative stretching and bending band strengths, we calibrated the linear dipole coefficients $\{\mu^s\}$ in Eq. (33) against the MD-derived 1D spectrum using a Bayesian hyperparameter search (TPE). Only the selected dipole parameters were varied while the MAB dynamical parameters were fixed, and the CHFPE 1D spectrum was recomputed in each trial. Because all spectra were normalized before comparison, the optimization targeted relative band strengths and lineshape rather than absolute intensity. The resulting best-fit $\{\mu^s\}$ were used in all subsequent 1D and 2D calculations.

The classical spectra obtained with the ML-parameterized MAB model closely reproduce the MD results, confirming the reliability of the parametrization. For both H_2O and D_2O , the stretching bands appear blue-shifted in the classical description because quantum anharmonic effects are absent.⁷⁵

Although the present MAB parameters were derived from classical MD trajectories, the underlying mb-p01 force field was originally developed for quantum nuclear dynamics. As a result, quantum HEOM-2DVS calculations using these parameters yield spectra that more closely resemble those expected from quantum-MD simulations and show better agreement with experiment than the classical results. A more rigorous validation of this approach will require MAB parameters trained directly on quantum-MD data.

Overall, aside from slight blue shifts, the HEOM-2DVS calculations based on the three-mode MAB model provide a reasonable description of the stretching and bending modes.

As experimentally observed, the linear absorption spectra of H_2O and D_2O differ because the heavier deuterium nuclei reduce the vibrational frequencies. Consequently, the O–D stretching and bending bands appear at much lower frequencies than the corresponding O–H modes. Moreover, the lighter H nuclei exhibit larger quantum fluctuations and faster hydrogen-bond dynamics, which broaden the absorption lines in H_2O , whereas D_2O shows narrower bands due to its slower structural fluctuations. In our numerical calculations, the low-vibration D_2O stretch mode exhibits suppressed quantum effects, resulting in both classical and quantum outcomes that more closely match experimental values.

1. 2D correlation IR spectra (quantum case)

We now present the quantum-mechanical calculation results for the 2D correlation IR spectra of H_2O and

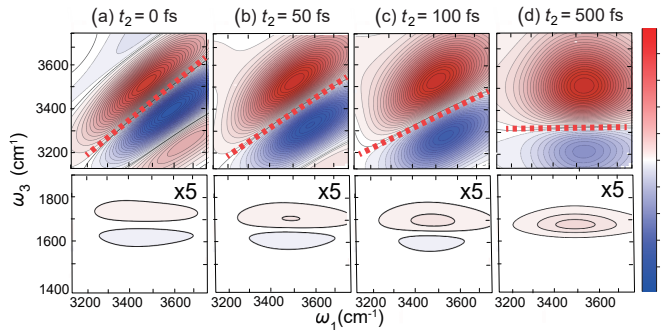


FIG. 3. The quantum-mechanically computed 2D correlation IR spectra of H₂O are shown for the stretching modes (1) and (1') in the upper panel, and for the coupled stretching (1, 1')-bending (2) motions in the lower panels. These spectra were obtained at several t_2 periods using the parameter sets listed in Tables I and II. The orientation of the red dashed nodal lines in the upper panel indicates the degree of correlation between the vibrational coherences during the t_1 and t_3 periods. For clarity, the contour interval in the lower panels has been increased by a factor of five.

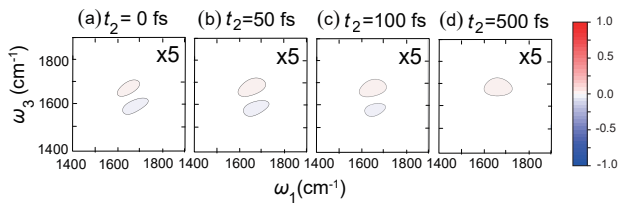


FIG. 4. The quantum-mechanically computed 2D correlation IR spectra of H₂O for the (2) bending motions were obtained using the parameter sets listed in Tables I and II. The spectral intensities were normalized to the maximum stretching amplitude. For emphasis, the peak intensity of the bending mode was multiplied by a factor of five relative to the intensity shown in Fig. 3.

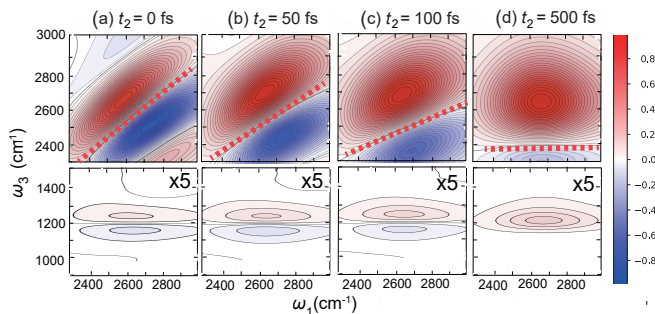


FIG. 5. The quantum-mechanically computed 2D correlation IR spectra of D₂O for the stretching modes (1) and (1') [upper panel] and the stretching (1, 1')-bending (2) motions [lower panels] at different t_2 periods. The orientation of the red dashed nodal lines in the upper panel indicates the degree of correlation between the vibrational coherences during the t_1 and t_3 periods. For emphasis, the contour interval in the lower panels was increased by a factor of five.

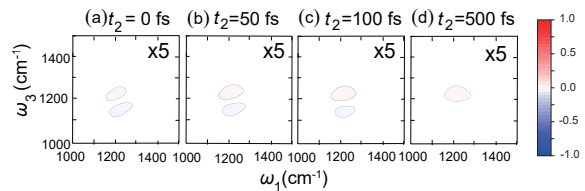


FIG. 6. The quantum-mechanically computed 2D correlation IR spectra of H₂O for the (2) bending motions using the parameter sets listed in Tables I and II. For emphasis, the peak intensity of the bending mode was multiplied by a factor of five relative to the intensity shown in Fig. 5.

D₂O using the three-mode MAB models whose parameter values are listed in Tables I and II. The corresponding classical results are provided in Appendix A.

While a number of experimental studies have reported 2D correlated IR spectra involving D₂O,^{6–18} whereas theoretical predictions that simultaneously treat all three intramolecular vibrational modes have remained scarce.^{24–34}

Figures 3 and 4 show the 2D correlation spectra of H₂O calculated at different t_2 periods.

Regarding the two stretching modes, the vibrational states are defined as $|0\rangle = |0\rangle_1 |0\rangle_{1'}$, $|1^\pm\rangle = (|1\rangle_1 |0\rangle_{1'} \pm |0\rangle_1 |1\rangle_{1'})/\sqrt{2}$, and $|2^\pm\rangle = (|2\rangle_1 |0\rangle_{1'} \pm |0\rangle_1 |2\rangle_{1'})/\sqrt{2}$. Then the major red and blue peaks can be assigned to the $|0\rangle \rightarrow |1^+\rangle \rightarrow |0\rangle$ and $|0\rangle \rightarrow |1^+\rangle \rightarrow |2^+\rangle$ pathways, respectively. The small blue and red peaks appear at the onset of the two major peaks originate from the $|0\rangle \rightarrow |1^-\rangle \rightarrow |0\rangle$, $|0\rangle \rightarrow |1^-\rangle \rightarrow |2^-\rangle$, and so forth.⁵³ These pathways proceed through coherent dynamics, with the associated peaks emerging immediately at $t_2 = 0$ and decaying as t_2 increases.

Such behavior differs from the 2D correlation IR spectrum calculated using CHFPE-2DVS with the two-mode MAB model and from the experimental spectrum in the limit of very small t_2 . This discrepancy is likely due to poorly optimized dipole elements and inter-stretch mode coupling being overestimated relative to the value obtained through the ML-optimized parametrization.

The orientation of the red dashed nodal lines reflects the degree of noise correlation (non-Markovian effects) between the vibrational coherences during t_1 and t_3 . A direction parallel to the ω_1 axis corresponds to the uncorrelated limit, whereas alignment along the $\omega_1 = \omega_3$ diagonal corresponds to the fully correlated limit.^{69–71} The diagonal peaks broaden along the $\omega_1 = \omega_3$ direction due to spectral diffusion driven by the slow noise correlation of the stretching coordinate. As t_2 increases beyond the noise correlation time ($\tau_1 \approx 160$ fs), the correlation between the t_1 and t_3 coherences weakens, and the nodal line gradually rotates toward the ω_1 axis, indicating a transition from correlated to uncorrelated fluctuations.

For the stretching→bending cross peaks, the peak shapes appear uncorrelated because the stretch→bend

noise correlation time is much shorter than that of stretch and bend themselves. As a result, the positive and negative cross peaks are elongated along the ω_1 direction. The cross-peak intensity decays at early times because it is dominated by coherence, but it subsequently increases once population transfer sets in.^{50,53}

Regarding the bending-mode results in Fig. 4, although the peak intensity is somewhat weaker than in the other calculations, the relaxation profile in the correlation spectrum is consistent with both the HEOM-2DVS results based on the POLI-2VS model⁵³ and the experimental observations.¹⁸

In D₂O results in Figs. 5 and 6, where the excitation frequencies of both the stretching and bending modes are lower than in H₂O, differences in the overall spectral profile are expected.

Excluding differences in spectral profiles arising from variations in the model, an examination of the contrast between H₂O and D₂O shows that, in D₂O, the narrower spacing between the stretch and bend modes leads to stronger stretch–bend coupling. This enhanced coupling facilitates more efficient energy transfer and consequently results in a slower decay of the cross peak.

The classical 2D correlation IR results evaluated using CHFPE-2DVS are summarized in Appendix A. The blue-shifted peak positions, the reduced linewidth broadening, and the clearer separation of the two stretching modes—features characteristic of classical calculations—appear consistently with previous computational studies.⁵¹ These spectra are expected to be close to those obtained by directly evaluating the nonlinear response function from MD trajectories. Although experimentally measured spectra naturally agree more closely with the quantum results, the classical 2DIR spectra remain useful because they approximate what would be obtained from a direct MD-based 2DIR calculation. In this sense, they provide a practical reference for extrapolating experimental trends from MD simulations.

V. CONCLUSION

In this study, we show that the condensed-phase dynamics of the intramolecular vibrations in H₂O and D₂O can be captured with unprecedented fidelity by integrating the `sbm14md` approach—which constructs MAB models directly from MD atomic trajectories—with the HEOM-2DVS and CHFPE-2DVS methods, which provide a numerically exact treatment of these models. The resulting linear absorption and 2D correlation IR spectra not only reproduce the essential experimental signatures but also expose striking isotope-dependent variations in anharmonicity, intermolecular coupling, and both energy and vibrational relaxation pathways. These features, largely inaccessible to conventional MD, underscore the critical importance of explicitly incorporating bath effects to accurately predict nonlinear spectroscopic responses.

Taken together, these results establish a unified mechanistic framework for vibrational dynamics in hydrogen-bonded liquids. By enabling systematic control over physical conditions—such as the character of environmental fluctuations or the presence of quantum effects—beyond the reach of standard MD simulations, the present approach offers a powerful route for disentangling the fundamental.

Because the `sbm14md` strategy employed here is intrinsically based on single MD trajectories, it can nevertheless be directly extended to solute molecules in solution, reaction centers in biomolecular environments, and other heterogeneous systems. By solving the quantum system using MAB model parameters determined from trajectories obtained via quantum MD and propagated with quantum HEOM, it becomes possible to incorporate quantum effects in a physically consistent manner. These directions represent promising avenues for future investigation.

ACKNOWLEDGMENTS

Y. T. was supported by JST (Grant No. CREST 1002405000170). K. P. acknowledges a fellowship supported by JST SPRING, the establishment of university fellowships toward the creation of science technology innovation (Grant No. JPMJSP2110).

AUTHOR DECLARATIONS

Conflict of Interest

The authors have no conflicts to disclose.

DATA AVAILABILITY

The data that support the findings of this study are available from the corresponding author upon reasonable request.

Appendix A: 2D correlation IR spectra (classical case)

Here, we present the classical mechanical 2D correlation IR spectra of H₂O (Figs. 7 and 8) and D₂O (Figs. 9 and 10) obtained using the classical CHFPE-2DVS method. These calculations employ the three mode MAB models, with parameter sets listed in Tables I and II.

The blue shifted peak positions, reduced linewidth broadening, and clearer separation of the two stretching modes, which are characteristic features of classical treatments, are consistent with previous computational studies.⁵¹

Compared with the quantum mechanical results for H₂O, the spectrum at $t_2 = 0$ differs markedly because

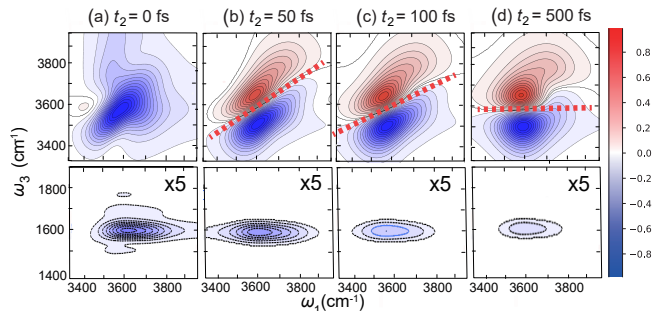


FIG. 7. The classical-mechanically computed 2D correlation IR spectra of H₂O for the stretching modes (1) and (1') [upper panel] and the stretching (1, 1')–bending (2) motions [lower panels] at different t_2 periods using the parameter sets listed in Tables I and II. The spectral intensities were normalized to the maximum stretching amplitude. For improved visibility, the contour interval in the lower panels—where the peak intensities are weaker—was increased by a factor of five.

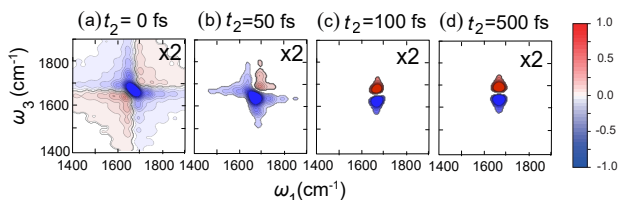


FIG. 8. The classical-mechanically calculated 2D correlation IR spectra of H₂O for the (2) bending motions using the parameter sets listed in Tables I and II. The spectral intensities were normalized to the maximum stretching amplitude. For emphasis, the peak intensity of the bending mode was multiplied by a factor of two relative to the intensity shown in Fig. 7.

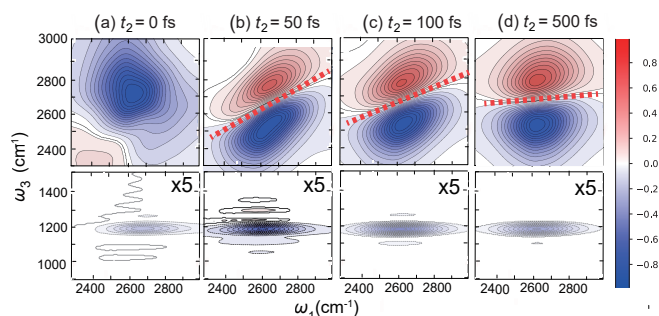


FIG. 9. The classical-mechanically computed 2D correlation IR spectra of D₂O for the stretching modes (1) and (1') [upper panel] and the stretching (1, 1')–bending (2) motions [lower panels] at different t_2 periods. For emphasis, the contour interval in the lower panels was increased by a factor of three.

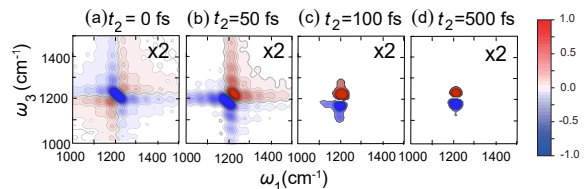


FIG. 10. The classical-mechanically computed 2D correlation IR spectra of H₂O for the (2) bending motions using the parameter sets listed in Tables I and II. The spectral intensities were normalized to the maximum stretching amplitude. For improved visibility, the contour interval in the lower panels—where the peak intensities are weaker—was increased by a factor of two.

coherent transitions are absent in the classical description. At larger t_2 values, the two vibrational modes become more clearly resolved, as quantum broadening is minimal.

In the classical case, the intensity of the stretch→bend cross peak also differs from the quantum result. Because only population relaxation contributes, the cross peak decays monotonically. The Bend peaks do not elongate over time because classical dynamics does not include the effects of coherence.

For low frequency D₂O, the results indicate that quantum effects are small. Thus, even the classical spectra show no substantial differences from the quantum ones, aside from the overall blue shift of the peaks and the behavior at $t_2 = 0$.

- ¹I. Ohmine and S. Saito, “Water dynamics : fluctuation, relaxation, and chemical reactions in hydrogen bond network rearrangement,” *Accounts of Chemical Research* **32**, 741–749 (1999).
- ²F. Paesani, “Water: Many-body potential for molecular simulations,” *Accounts of Chemical Research* **52**, 273–281 (2019), review of molecular modeling approaches including isotope effects in hydrogen bonding.
- ³S. Cukierman, “Et tu, grothuss! and other unfinished stories,” *Biochimica et Biophysica Acta (BBA) - Bioenergetics* **1757**, 876–885 (2006), review of proton transfer and isotope effects in hydrogen-bonded networks.
- ⁴A. Kohen and H.-H. Limbach, *Isotope Effects in Chemistry and Biology* (CRC Press, 2010) extensive reference on kinetic isotope effects and their role in chemical mechanisms.
- ⁵R. Guillemin et al., “Isotope effects in dynamics of water isotopologues induced by core ionization at an x-ray free-electron laser,” *Struct. Dyn.* **10**, 054302 (2023).
- ⁶M. Cowan, B. Bruner, N. Huse, J. Dwyer, B. Chugh, E. Nibbering, T. Elsaesser, and R. Miller, “Ultrafast memory loss and energy redistribution in the hydrogen bond network of liquid H₂O,” *NATURE* **434**, 199–202 (2005).
- ⁷N. Huse, S. Ashihara, E. Nibbering, and T. Elsaesser, “Ultrafast vibrational relaxation of O-H bending and librational excitations in liquid H₂O,” *CHEMICAL PHYSICS LETTERS* **404**, 389–393 (2005).
- ⁸D. Kraemer, M. L. Cowan, A. Paarmann, N. Huse, E. T. J. Nibbering, T. Elsaesser, and R. J. D. Miller, “Temperature dependence of the two-dimensional infrared spectrum of liquid H₂O,” *Proceedings of the National Academy of Sciences* **105**, 437–442 (2008).

- ⁹A. Tokmakoff, "Two-dimensional infrared spectroscopy of water," *J. Chem. Phys.* **116**, 5563–5579 (2002).
- ¹⁰C. Fecko, J. Eaves, J. Loparo, A. Tokmakoff, and P. Geissler, "Ultrafast hydrogen-bond dynamics in the infrared spectroscopy of water," *SCIENCE* **301**, 1698–1702 (2003).
- ¹¹J. D. Eaves, A. Tokmakoff, and P. L. Geissler, "Electric field fluctuations drive vibrational dephasing in water," *The Journal of Physical Chemistry A* **109**, 9424–9436 (2005), pMID: 16866391.
- ¹²M. Thämer, L. D. Marco, K. Ramasesha, A. Mandal, and A. Tokmakoff, "Ultrafast 2d IR spectroscopy of the excess proton in liquid water," *Science* **350**, 78–82 (2015).
- ¹³L. De Marco, J. A. Fournier, M. Thämer, W. Carpenter, and A. Tokmakoff, "Anharmonic exciton dynamics and energy dissipation in liquid water from two-dimensional infrared spectroscopy," *The Journal of Chemical Physics* **145**, 094501 (2016), <https://aip.scitation.org/doi/pdf/10.1063/1.4961752>.
- ¹⁴L. De Marco, W. Carpenter, H. Liu, R. Biswas, J. M. Bowman, and A. Tokmakoff, "Differences in the vibrational dynamics of h₂o and d₂o: Observation of symmetric and antisymmetric stretching vibrations in heavy water," *The Journal of Physical Chemistry Letters* **7**, 1769–1774 (2016), pMID: 27115316.
- ¹⁵N. H. C. Lewis, B. Dereka, Y. Zhang, E. J. Maginn, and A. Tokmakoff, "From networked to isolated: Observing water hydrogen bonds in concentrated electrolytes with two-dimensional infrared spectroscopy," *The Journal of Physical Chemistry B* **126**, 5305–5319 (2022), pMID: 35829623, <https://doi.org/10.1021/acs.jpcc.2c03341>.
- ¹⁶A. A. Bakulin, C. Liang, T. la Cour Jansen, D. A. Wiersma, H. J. Bakker, and M. S. Pshenichnikov, "Hydrophobic solvation: A 2d ir spectroscopic inquest," *Accounts of Chemical Research* **42**, 1229–1238 (2009), <https://doi.org/10.1021/ar9000247>.
- ¹⁷P. Hamm and M. Zanni, *Concepts and Methods of 2D Infrared Spectroscopy* (Cambridge University Press, 2011) comprehensive reference on experimental 2D IR methods applied to water and isotope effects.
- ¹⁸L. Chuntonov, R. Kumar, and D. G. Kuroda, "Non-linear infrared spectroscopy of the water bending mode: direct experimental evidence of hydration shell reorganization?" *Phys. Chem. Chem. Phys.* **16**, 13172–13181 (2014).
- ¹⁹T. Yagasaki and S. Saito, "Fluctuations and relaxation dynamics of liquid water revealed by linear and nonlinear spectroscopy," *Annual Review of Physical Chemistry* **64**, 55–75 (2013), <https://doi.org/10.1146/annurev-physchem-040412-110150>.
- ²⁰T. Yagasaki and S. Saito, "Ultrafast intermolecular dynamics of liquid water: A theoretical study on two-dimensional infrared spectroscopy," *The Journal of Chemical Physics* **128**, 154521 (2008), <https://doi.org/10.1063/1.2903470>.
- ²¹B. Auer, R. Kumar, J. R. Schmidt, and J. L. Skinner, "Hydrogen bonding and raman, ir, and 2d-ir spectroscopy of dilute hod in liquid d₂o," *Proceedings of the National Academy of Sciences* **104**, 14215–14220 (2007).
- ²²T. I. C. Jansen, B. M. Auer, M. Yang, and J. L. Skinner, "Two-dimensional infrared spectroscopy and ultrafast anisotropy decay of water," *The Journal of Chemical Physics* **132**, 224503 (2010).
- ²³T. I. C. Jansen, S. Saito, J. Jeon, and M. Cho, "Theory of coherent two-dimensional vibrational spectroscopy," *The Journal of Chemical Physics* **150**, 100901 (2019), <https://doi.org/10.1063/1.5083966>.
- ²⁴R. Rey, K. B. Møller, and J. T. Hynes, "Hydrogen bond dynamics in water and ultrafast infrared spectroscopy," *The Journal of Physical Chemistry A* **106**, 11993–11996 (2002).
- ²⁵C. P. Lawrence and J. L. Skinner, "Vibrational spectroscopy of hod in liquid d₂o. I. vibrational energy relaxation," *The Journal of Chemical Physics* **117**, 5827–5838 (2002).
- ²⁶C. P. Lawrence and J. L. Skinner, "Vibrational spectroscopy of hod in liquid d₂o. II. infrared line shapes and vibrational stokes shift," *The Journal of Chemical Physics* **117**, 8847–8854 (2002).
- ²⁷C. P. Lawrence and J. L. Skinner, "Vibrational spectroscopy of hod in liquid d₂o. III. spectral diffusion, and hydrogen-bonding and rotational dynamics," *The Journal of Chemical Physics* **118**, 264–272 (2003).
- ²⁸A. Piryatinski, C. P. Lawrence, and J. L. Skinner, "Vibrational spectroscopy of hod in liquid d₂o. iv. infrared two-pulse photon echoes," *The Journal of Chemical Physics* **118**, 9664–9671 (2003).
- ²⁹A. Piryatinski, C. P. Lawrence, and J. L. Skinner, "Vibrational spectroscopy of HOD in liquid D₂O. v. infrared three-pulse photon echoes," *The Journal of Chemical Physics* **118**, 9672–9679 (2003), <https://doi.org/10.1063/1.1569474>.
- ³⁰S. A. Corcelli, C. P. Lawrence, and J. L. Skinner, "Combined electronic structure/molecular dynamics approach for ultrafast infrared spectroscopy of dilute hod in liquid h₂o and d₂o," *The Journal of Chemical Physics* **120**, 8107–8117 (2004).
- ³¹S. A. Corcelli and J. L. Skinner, "Infrared and raman line shapes of dilute hod in liquid h₂o and d₂o from 10 to 90°c," *The Journal of Physical Chemistry A* **109**, 6154–6165 (2005), pMID: 16833955.
- ³²C. J. Fecko, J. D. Eaves, J. J. Loparo, A. Tokmakoff, and P. L. Geissler, "Ultrafast hydrogen-bond dynamics in the infrared spectroscopy of water," *Science* **301**, 1698–1702 (2003), <https://www.science.org/doi/pdf/10.1126/science.1087251>.
- ³³T. I. C. Jansen, D. Cringus, and M. S. Pshenichnikov, "Dis-similar dynamics of coupled water vibrations," *The Journal of Physical Chemistry A* **113**, 6260–6265 (2009), pMID: 19438222, <https://doi.org/10.1021/jp900480r>.
- ³⁴W. B. Carpenter, J. A. Fournier, R. Biswas, G. A. Voth, and A. Tokmakoff, "Delocalization and stretch-bend mixing of the HOH bend in liquid water," *The Journal of Chemical Physics* **147**, 084503 (2017), <https://doi.org/10.1063/1.4987153>.
- ³⁵J. Liu, W. H. Miller, G. S. Fanourgakis, S. S. Xantheas, S. Imoto, and S. Saito, "Insights in quantum dynamical effects in the infrared spectroscopy of liquid water from a semiclassical study with an ab initio-based flexible and polarizable force field," *The Journal of Chemical Physics* **135**, 244503 (2011), <https://doi.org/10.1063/1.3670960>.
- ³⁶S. Imoto, S. S. Xantheas, and S. Saito, "Ultrafast dynamics of liquid water: Frequency fluctuations of the OH stretch and the HOH bend," *The Journal of Chemical Physics* **139**, 044503 (2013), <https://doi.org/10.1063/1.4813071>.
- ³⁷S. Imoto, S. S. Xantheas, and S. Saito, "Ultrafast dynamics of liquid water: Energy relaxation and transfer processes of the OH stretch and the HOH bend," *The Journal of Physical Chemistry B* **119**, 11068–11078 (2015), pMID: 26042611, <https://doi.org/10.1021/acs.jpcc.5b02589>.
- ³⁸V. Babin, C. Leforestier, and F. Paesani, "Development of a "first principles" water potential with flexible monomers: Dimer potential energy surface, VRT spectrum, and second virial coefficient," *Journal of Chemical Theory and Computation* **9**, 5395–5403 (2013), pMID: 26592277.
- ³⁹V. Babin, G. R. Medders, and F. Paesani, "Development of a "first principles" water potential with flexible monomers. II: Trimer potential energy surface, third virial coefficient, and small clusters," *Journal of Chemical Theory and Computation* **10**, 1599–1607 (2014), pMID: 26580372.
- ⁴⁰M. Rossi, H. Liu, F. Paesani, J. Bowman, and M. Ceriotti, "Communication: On the consistency of approximate quantum dynamics simulation methods for vibrational spectra in the condensed phase," *The Journal of Chemical Physics* **141**, 181101 (2014), <https://doi.org/10.1063/1.4901214>.
- ⁴¹G. R. Medders, V. Babin, and F. Paesani, "Development of a "first-principles" water potential with flexible monomers. iii. liquid phase properties," *Journal of Chemical Theory and Computation* **10**, 2906–2910 (2014), pMID: 26588266, <https://doi.org/10.1021/ct5004115>.
- ⁴²K. M. Hunter, F. A. Shakib, and F. Paesani, "Disentangling coupling effects in the infrared spectra of liquid water," *The Journal of Physical Chemistry B* **122**, 10754–10761 (2018), pMID: 30403350, <https://doi.org/10.1021/acs.jpcc.8b09910>.
- ⁴³X. Liu and J. Liu, "Critical role of quantum dy-

- namical effects in the Raman spectroscopy of liquid water,” *Molecular Physics* **116**, 755–779 (2018), <https://doi.org/10.1080/00268976.2018.1434907>.
- ⁴⁴G. Trenins, M. J. Willatt, and S. C. Althorpe, “Path-integral dynamics of water using curvilinear centroids,” *The Journal of Chemical Physics* **151**, 054109 (2019), <https://doi.org/10.1063/1.5100587>.
- ⁴⁵S. Ueno and Y. Tanimura, “Modeling intermolecular and intramolecular modes of liquid water using multiple heat baths: Machine learning approach,” *Journal of Chemical Theory and Computation* **16**, 2099–2108 (2020).
- ⁴⁶K. Park, J.-Y. Jo, and Y. Tanimura, “System–bath modeling in vibrational spectroscopy via molecular dynamics: A machine learning framework for hierarchical equations of motion (heom),” *The Journal of Chemical Physics* **163**, 214104 (2025).
- ⁴⁷K. Park, S. Ueno, and Y. Tanimura, “sbml4md: A computational platform for system–bath modeling via molecular dynamics powered by machine learning,” *The Journal of Chemical Physics* **164**, 082502 (2026).
- ⁴⁸A. Ishizaki and Y. Tanimura, “Nonperturbative non-Markovian quantum master equation: Validity and limitation to calculate nonlinear response functions,” *Chemical Physics* **347**, 185–193 (2008), *ultrafast Photoinduced Processes in Polyatomic Molecules*.
- ⁴⁹H. Takahashi and Y. Tanimura, “Discretized hierarchal equations of motion in mixed Liouville–Wigner space for two-dimensional vibrational spectroscopies of water,” *The Journal of Chemical Physics* **158**, 044115 (2023), [arXiv:2302.09799](https://arxiv.org/abs/2302.09799).
- ⁵⁰H. Takahashi and Y. Tanimura, “Simulating two-dimensional correlation spectroscopies with third-order infrared and fifth-order infrared–Raman processes of liquid water,” *The Journal of Chemical Physics* **158**, 124108 (2023), [arXiv:2302.09760](https://arxiv.org/abs/2302.09760).
- ⁵¹R. Hoshino and Y. Tanimura, “Analysis of intramolecular modes of liquid water in two-dimensional spectroscopy: A classical hierarchical equations of motion approach,” *The Journal of Chemical Physics* **162**, 044105 (2025), https://pubs.aip.org/aip/jcp/article-pdf/doi/10.1063/5.0245564/20360227/044105_1.5.0245564.pdf.
- ⁵²R. Hoshino and Y. Tanimura, “A multimode classical hierarchical Fokker–Planck equations approach to molecular vibrations: Simulating two-dimensional spectra,” *The Journal of Chemical Physics* **163**, 172501 (2025).
- ⁵³R. Hoshino and Y. Tanimura, “HEOM-based numerical framework for quantum simulation of two-dimensional vibrational spectra in molecular liquids (heom-2dvs),” *The Journal of Chemical Physics* **16x**, xxxx (2026).
- ⁵⁴T. Ikeda, H. Ito, and Y. Tanimura, “Analysis of 2D THz-Raman spectroscopy using a non-Markovian Brownian oscillator model with nonlinear system–bath interactions,” *The Journal of Chemical Physics* **142**, 212421 (2015).
- ⁵⁵H. Ito and Y. Tanimura, “Simulating two-dimensional infrared-Raman and Raman spectroscopies for intermolecular and intramolecular modes of liquid water,” *The Journal of Chemical Physics* **144**, 074201 (2016).
- ⁵⁶K. Okumura and Y. Tanimura, “The $(2n+1)$ th-order off-resonant spectroscopy from the $(n+1)$ th-order anharmonicities of molecular vibrational modes in the condensed phase,” *The Journal of Chemical Physics* **106**, 1687–1698 (1997).
- ⁵⁷Y. Tanimura, “Stochastic Liouville, Langevin, Fokker–Planck, and master equation approaches to quantum dissipative systems,” *Journal of the Physical Society of Japan* **75**, 082001 (2006).
- ⁵⁸Y. Tanimura, “Numerically “exact” approach to open quantum dynamics: The hierarchical equations of motion (HEOM),” *The Journal of Chemical Physics* **153**, 020901 (2020).
- ⁵⁹Y. Tanimura and P. G. Wolynes, “Quantum and classical Fokker–Planck equations for a Gaussian–Markovian noise bath,” *Phys. Rev. A* **43**, 4131–4142 (1991).
- ⁶⁰K. Okumura and Y. Tanimura, “Two-time correlation functions of a harmonic system nonbilinearly coupled to a heat bath: Spontaneous Raman spectroscopy,” *Phys. Rev. E* **56**, 2747–2750 (1997).
- ⁶¹Y. Tanimura and S. Mukamel, “Two-dimensional femtosecond vibrational spectroscopy of liquids,” *The Journal of Chemical Physics* **99**, 9496–9511 (1993).
- ⁶²Y. Tanimura, “Fifth-order two-dimensional vibrational spectroscopy of a Morse potential system in condensed phases,” *Chemical Physics* **233**, 217–229 (1998).
- ⁶³Y. Tanimura and T. Steffen, “Two-dimensional spectroscopy for harmonic vibrational modes with nonlinear system–bath interactions.ii. Gaussian–Markovian case,” *Journal of the Physical Society of Japan* **69**, 4095–4106 (2000).
- ⁶⁴T. Kato and Y. Tanimura, “Two-dimensional Raman and infrared vibrational spectroscopy for a harmonic oscillator system nonlinearly coupled with a colored noise bath,” *The Journal of Chemical Physics* **120**, 260–271 (2004).
- ⁶⁵H. Ito, J.-Y. Jo, and Y. Tanimura, “Notes on simulating two-dimensional Raman and terahertz-Raman signals with a full molecular dynamics simulation approach,” *Structural Dynamics* **2**, 054102 (2015).
- ⁶⁶T. Hasegawa and Y. Tanimura, “Nonequilibrium molecular dynamics simulations with a backward-forward trajectories sampling for multidimensional infrared spectroscopy of molecular vibrational modes,” *The Journal of Chemical Physics* **128**, 064511 (2008).
- ⁶⁷T. Hasegawa and Y. Tanimura, “A polarizable water model for intramolecular and intermolecular vibrational spectroscopies,” *The Journal of Physical Chemistry B* **115**, 5545–5553 (2011).
- ⁶⁸J. Hu, R.-X. Xu, and Y. Yan, “Communication: Padé spectrum decomposition of Fermi function and Bose function,” *The Journal of Chemical Physics* **133**, 101106 (2010).
- ⁶⁹J. D. Hybl, A. Albrecht Ferro, and D. M. Jonas, “Two-dimensional fourier transform electronic spectroscopy,” *The Journal of Chemical Physics* **115**, 6606–6622 (2001), <https://doi.org/10.1063/1.1398579>.
- ⁷⁰N.-H. Ge, M. T. Zanni, and R. M. Hochstrasser, “Effects of vibrational frequency correlations on two-dimensional infrared spectra†,” *Journal of Physical Chemistry A* **106**, 962–972 (2002).
- ⁷¹M. Khalil, N. Demirdöven, and A. Tokmakoff, “Obtaining absorptive line shapes in two-dimensional infrared vibrational correlation spectra,” *Phys. Rev. Lett.* **90**, 047401 (2003).
- ⁷²Y. Litman, V. Kapil, Y. M. Y. Feldman, D. Tisi, T. Begušić, K. Fidanyan, G. Fraux, J. Higer, M. Kellner, T. E. Li, E. S. Pósz, E. Stocco, G. Trenins, B. Hirshberg, M. Rossi, and M. Ceriotti, “i-pi 3.0: a flexible and efficient framework for advanced atomistic simulations,” *J. Chem. Phys.* **161**, 062505 (2024).
- ⁷³Y. Maréchal, “The molecular structure of liquid water delivered by absorption spectroscopy in the whole IR region completed with thermodynamics data,” *Journal of Molecular Structure* **1004**, 146–155 (2011).
- ⁷⁴J.-J. Max and C. Chapados, “Isotope effects in liquid water by infrared spectroscopy. iii. h₂o and d₂o spectra from 6000 cm⁻¹,” *The Journal of Chemical Physics* **131**, 184505 (2009).
- ⁷⁵A. Sakurai and Y. Tanimura, “Does \hbar play a role in multidimensional spectroscopy? reduced hierarchy equations of motion approach to molecular vibrations,” *The Journal of Physical Chemistry A* **115**, 4009–4022 (2011).